Thermoelectric Performance of n-Type Magnetic Element Doped Bi2S3

FORTULAN, R, AMINORROAYA YAMINI, Sima <http://orcid.org/0000-0002-2312-8272>, NWANEBU, C, LI, S, BABA, T, REECE, MJ <http://orcid.org/0000-0002-2293-7123> and MORI, T <http://orcid.org/0000-0003-2682-1846>

Thermoelectric performance of *n*-type magnetic element doped Bi_2S_3

Raphael Fortulan[a], Sima Aminorroaya Yamini[a,b]*, Chibuzor Nwanebu[a], Suwei Li[c], Takahiro Baba[d,e], Michael John Reece[c], Takao Mori[d,e]

[a] Materials and Engineering Research Institute, Sheffield Hallam University, Sheffield S1 1WB, UK

[b] Department of Engineering and Mathematics, Sheffield Hallam University, Sheffield S1 1 WB, UK

[c] School of Engineering and Material Science, Queen Mary University of London, Mile End Road, London, E1 4NS, UK

[d] International Center for Materials Nanoarchitectonics (WPI-MANA), National Institute for Materials Science, Tsukuba, 305-0044, Japan

[e] Graduate School of Pure and Applied Science, University of Tsukuba, Tsukuba, 305-8577, Japan

*Email: S.Aminorroaya@shu.ac.uk

ABSTRACT: Thermoelectric technology offers great potential for converting waste heat into electrical energy and is an emission-free technique for solid-state cooling. Conventional high performance thermoelectric materials such as Bi_2Te_3, PbTe use rare or toxic elements. Sulphur is an inexpensive and non-toxic alternative to tellurium. However, achieving high efficiencies with Bi_2S_3 is challenging due to its high electrical resistivity that reduces its power factor. Here, we report Bi_2S_3 co-doped with Cr and Cl to enhance its thermoelectric properties. An enhanced conductivity was achieved due to an increase in the carrier concentration by the substitution of S with Cl. High values of the Seebeck coefficients were obtained despite high carrier concentrations, this is attributed to an increase in the effective mass, resulted from the magnetic drag introduced by the magnetic Cr dopant. A peak power factor of 566 μW m^{-1} K^{-2} was obtained for cast sample of $Bi_{2-x/3}Cr_{x/3}S_{3-x}Cl_x$ with x = 0.01 at 320 K, as high as the largest values reported in literature for the sintered samples. These results support the success of co-doping thermoelectric materials with isovalent magnetic and carrier concentration tuning elements to enhance the thermoelectric properties of eco-friendly materials.

KEYWORDS: *thermoelectric, power factor, magnetic element, bismuth sulphide, chromium*

INTRODUCTION

Solid-state based thermoelectric (TE) materials can directly and reversibly convert heat into electricity. The efficiency of thermoelectric materials is given by the figure of merit, $zT = (S^2T)/\rho\kappa_{total}$, where S is the Seebeck coefficient, T is the absolute temperature, ρ is the electrical resistivity, and κ_{total} is the thermal conductivity.

To increase zT, one needs to increase the power factor (S^2/ρ) and/or decrease κ_{total}. One of the most successful approaches to improve the figure of merit is reducing the lattice thermal conductivity, and over the years, various phonon engineering approaches have been used to enhance phonon scattering and decrease κ_L by taking advantage of nanoprecipitates [1,2], alloying elements [3,4], nanostructured grain boundaries [5,6] and ionised impurities [7,8].

A series of band structure engineering approaches have also been employed to improve the power factor of TE materials [9–11]. Strategies such as quantum confinement [12], modulation doping [13–15], and energy filtering [16,17]are being actively pursued.

Magnetic interactions have been proposed as a strategy to enhance the Seebeck coefficient in thermoelectric materials such as Bi_2Te_3 [18–23]. Charge carriers interact with the local magnetic moments, effectively drag the carriers, which results in an increased charge carrier effective mass, increasing the Seebeck coefficient, and decreasing carrier mobility (μ). Overall, this has resulted in an increased power factor [18–24].

Tellurium based thermoelectric materials such as Bi_2Te_3 have been employed as power generators/refrigerators in lower temperature applications (< 500 K). However, tellurium is expensive, rare and can hinder the movement towards mass adoption of TE generators. Sulphur, another element from group IV, is inexpensive, non-toxic, and a sustainable alternative. Bismuth sulphide (Bi_2S_3), in particular, has low thermal conductivity and a large Seebeck coefficient [25,26]. However, its high resistivity results in a low zT [27]. Several dopants have been used to optimise the electronic transport properties of Bi_2S_3, including $CuBr_2$ [28], Sb [29], Cu [30], Ag [31], I [32], Cl [33], Se [33,34], $InCl_3$ [35], $BiCl_3$ [36], and $NbCl_5$ [37]. A lower thermal conductivity was also obtained in Bi_2S_3 by nano structuring [30,38–40].

The thermoelectric efficiency of pristine Bi_2S_3 was also increased to 0.11 from 0.09 at 623 K by texturing through hot-forging and introducing sulphur vacancies [41]. $PbBr_2$ doping of bulk Bi_2S_3 has significantly improved its electrical conductivity by modulation doping, and reduced the lattice thermal conductivity by introducing nanoprecipitates, resulting in a peak zT value of 0.8 at 673 K [42].

It has been widely shown that the charge density is increased when halogen group elements (Cl, Br, and I) are

doped at the sulphur sites [28,32,33]. Here, we doped bismuth sulphide with chromium chloride ($CrCl_3$) to obtain samples of $Bi_{2-x/3}Cr_{x/3}S_{3-x}Cl_x$ (x = 0.00, 0.005, 0.01, 0.015, 0.02). Doping with chlorine increases the number of free carriers in the material, leading to a reduction in the electrical resistivity, while the magnetic effect of chromium resulted to an increase in the carrier effective mass and, consequently, in the Seebeck coefficient.

EXPERIMENTAL SECTION

Samples Fabrication. Ultra-high purity bismuth pieces (99.999%, Sigma Aldrich), sulphur pieces (99.9995%, Alfa Aesar Puratronic) and chromium chloride powder (99.99%, Sigma Aldrich) were mixed stoichiometrically to obtain $Bi_{2-x/3}Cr_{x/3}S_{3-x}Cl_x$ (x = 0.00, 0.005, 0.01, 0.015, 0.02) in vacuum-sealed quartz ampoules, prepared in an inert atmosphere glove box. The tubes were heated in a tube furnace to 1000 °C. After being quenched in cold water, the samples were annealed at 450°C for 2 days.

The cylindrical ingot samples of 10 mm diameter were then cut into disk shapes of 10 mm in diameter and ~1.5 mm thickness, for Hall effect measurements, and bars of 2 × 2 × 10 mm^3 for electrical properties measurements. The electrical resistivity and Seebeck coefficient were measured simultaneously under 0.1 bar of helium from room temperature to 483 K using an LSR - 3 Linseis unit. Hall effect measurements were performed in an Ecopia HMS-3000 Hall Measurement System at room temperature. The density of the samples was determined from the bar-shaped samples using theirs dimensions and mass. All samples were then manually ground to fine powders by using an agate mortar and pestle. Three samples with x = 0, 0.005, and 0.01 were sintered in a 10 mm diameter graphite die under an axial pressure of 63 MPa at 723 K for 5 minutes under the vacuum, the sample with x = 0.01 broke during sintering. To avoid this, the sintering temperature was reduced to 623 K for the samples with composition of x = 0.015 and 0.02. The measured densities of all samples are presented in Tables S1 and S2, Supporting Information.

Material Characterisation. To investigate the electrical and thermal transport properties parallel and perpendicular to the sintering direction, the sintered samples were cut and polished into disks (10 mm in diameter and ~1.5 mm thickness, perpendicular to the pressing direction) and cuboidal of 8 × 8 × 2 mm^3, parallel to the pressing direction for Hall effect and thermal diffusivity measurements, and bars of 2 × 2 × 10 mm^3 (parallel and perpendicular to the pressing direction) for electrical properties measurements. The total thermal conductivity (κ_{total}) was calculated from the thermal diffusivity (D), heat capacity (C_p) and density (ρ), $\kappa_{total} = D \cdot C_p \cdot \rho$. The temperature-dependent thermal diffusivity D was measured on disc-shaped samples using the laser flash diffusivity method using LFA-467 Hyperflash, Netzsch. The temperature-dependent heat capacity was derived using a standard sample (Pyroceram-9060). The directions of measurement and sample shapes are illustrated in Figure 1. X-ray powder diffraction analysis was performed by X'Pert PRO, PANalytical using Cu-Kα1 radiation (λ = 1.54059 Å) to identify the crystal structure of each sample. Rietveld refinement was performed using GSAS-II [43] to obtain the lattice parameters for all samples.

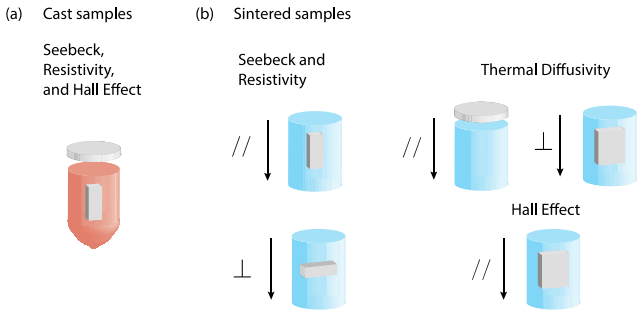

Figure 1. Measuring directions and sample shapes of the (a) Cast samples and (b) Sintered samples.

Electronic Structure Calculation. Density Functional Theory (DFT) calculations were employed to qualitatively study the electronic band structure of the doped sample. The Perdew–Burke–Ernzerhof (PBE) and generalized gradient approximation (GGA) exchange-correlation functionals were used [44] with the Quantum Espresso package [45]. Monkhorst–Pack procedure was used to generate 12 x 12 x 12 k-points for the Brillouin zone [46]. The plane wave/pseudopotential approach was employed, with a kinetic energy cut-off of 45 Ry for the wavefunctions and 360 Ry for the electron density. Spin polarization was considered for the materials doped with Cr.

RESULTS AND DISCUSSION

Materials Characteristics. Figure 2 shows the XRD patterns of samples $Bi_{2-x/3}Cr_{x/3}S_{3-x}Cl_x$ (x = 0.00, 0.005, 0.01, 0.015, 0.02). All patterns confirm the presence of a single phase Bi_2S_3, orthorhombic crystal structure with Pnma space group. The lattice parameters of all the samples were determined by the Rietveld refinement of the XRD patterns (Table S3, Supporting Information). No variation of the lattice parameters was detected, due to comparable ionic radius of S^{2-} (1.84 Å) and Cl^{1-} (1.81 Å) [47]. Although there is a difference in the ionic radii of Bi^{3+} (1.03 Å) and Cr^{+3} (0.615 Å) [47], the amount of chromium introduced to the Bi_2S_3 is one-third of chlorine atomic ratio, and therefore no noticeable difference was detected in the lattice parameters.

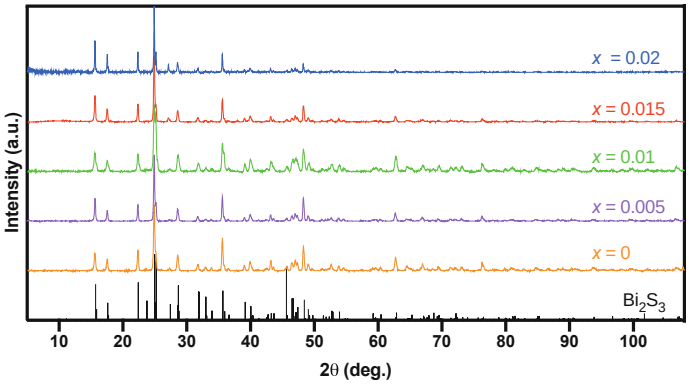

Figure 2. Powder XRD Patterns of $Bi_{2-x/3}Cr_{x/3}S_{3-x}Cl_x$ (x = 0.00, 0.005, 0.01, 0.015, 0.02) samples in the range of 5° to 108°.

The lattice parameter values are consistent with the values reported in the literature (a = 11.269 Å, b = 3.972Å, and c = 11.129 Å) [48].

The intensity of the {111} plane peaks for the x = 0.015 sample was higher than for the other samples. This might be attributed to preferred orientation, caused by non-uniform hand milling of the samples used for the XRD analysis.

The XRD analysis was also performed on the sintered samples (Figure S1 of Supporting Information), and the lattice parameters were calculated by Rietveld refinement (Table S4, Supporting Information). The lattice parameter values of $Bi_{2-x/3}Cr_{x/3}S_{3-x}Cl_x$ (x = 0.00, 0.005, 0.01, 0.015, 0.02) samples versus the dopant concentration (x) of cast and sintered samples are shown in Figure 3.

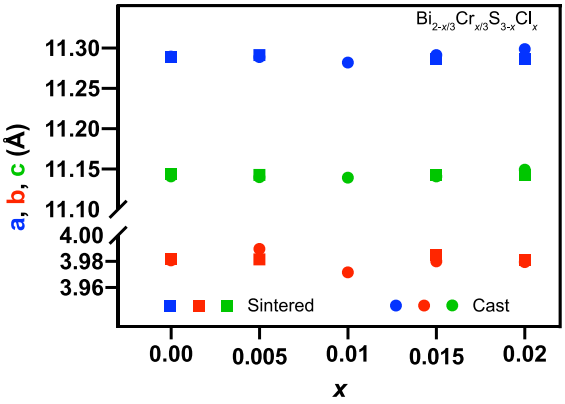

Figure 3. Rietveld refined lattice parameters of $Bi_{2-x/3}Cr_{x/3}S_{3-x}Cl_x$ (x = 0.00, 0.005, 0.01, 0.015, 0.02) samples as a function of the dopant concentration.

To understand the effect of dopants on the electronic band structure of Bi_2S_3, the band structure of Bi_2S_3 and doped sample of $Bi_{23}Cr_1S_{33}Cl_3$, for spin-up and -down states, were calculated (Figure 4(a), (b), and (c), respectively). The calculated bandgap of the pristine material is ~1.25 eV, which is in good agreement with the reported experimental values of ~1.3 eV [35,49,50]. Both spin-up and spin-down states showed a reduced value of ~0.6 eV and ~0.92 eV, respectively. The reduction in the band gap for the spin-up state was due the presence of an additional impurity band. It is worth noting that the numerical results, presented in this calculation, should only be discussed qualitatively due to the rather high concentration of dopant. The effective masses of electrons were calculated for both heavy and light bands in the spin-up (D point) and spin-down (Γ point) states of the electronic band structures, using the parabolic band approximation for the bands extrema. The results are shown in Figure S2, Supporting Information. The electrons of both heavy and light bands show similar values of effective mass ($m^*_{heavy} \approx 0.48$ and $m^*_{light} \approx 0.41$ for the spin-up and $m^*_{heavy} \approx 0.35$ and $m^*_{light} \approx 0.21$ for spin-down state), indicating that the electronic band degeneracy plays an insignificant role in the transport properties of the material.

Electronic Transport Properties. The Seebeck coefficient, the electrical resistivity, and the carrier concentration of the cast samples of $Bi_{2-x/3}Cr_{x/3}S_{3-x}Cl_x$ (x = 0.00, 0.005, 0.01, 0.015, 0.02) and sintered samples of $Bi_{2-x/3}Cr_{x/3}S_{3-x}Cl_x$ (x = 0.00, 0.005, 0.015, 0.02) measured parallel to the direction of sintering are presented in Figure 5. The negative Seebeck coefficient indicates an n-type semiconductor behaviour (Figure 5(a) and (b)). The Seebeck coefficient for the cast pristine Bi_2S_3 sample ranges from -96 μV K^{-1} at ~320 K to -135 μV K^{-1} at ~480 K. These values are considerably smaller than the reported values of -380 to 498 μV K^{-1} for Bi_2S_3 in the literature [26,38]. Following Mott's formula for the Seebeck coefficient [51], $S = \left(\frac{\pi^2 k_B^2 T}{3q}\right)\left\{\frac{d n(E)}{dE}\frac{1}{n} + \frac{d\mu(E)}{dE}\frac{1}{\mu}\right\}_{E=E_F}$, the sharp decrease in the Seebeck coefficient can be explained by an increase in the charge carrier density in the material. This is supported by the electrical resistivity values for these samples, which varied from 3.16 mΩ cm at ~320 K to -4.82 mΩ cm at ~480 K (Figure 5(c)). These values, including for x=0, are significantly smaller than the reported values of ~2400 mΩ cm [41] and ~7460 mΩ cm [52] for the pristine sample of Bi_2S_3. These results can be explained by the volatile nature of sulphur during the sample fabrication. A single sulphur atom vacancy donates 2 free electrons to the bulk material. Atom vacancies in bismuth sulphide have been previously reported [37,38] and it commonly occurs in chalcogenides [53,54]. This is supported by the high charge carrier concentrations measured for both cast and sintered samples (Figure 5(e) and (f)). This also greatly reduces the resistivity for the heavily doped samples reaching 4.82 mΩ cm at ~480 K for x = 0.02 compared to 7.46 mΩ cm for the pristine sample at room temperature. No significant difference was observed in the Seebeck coefficient values of sintered samples for both measurement

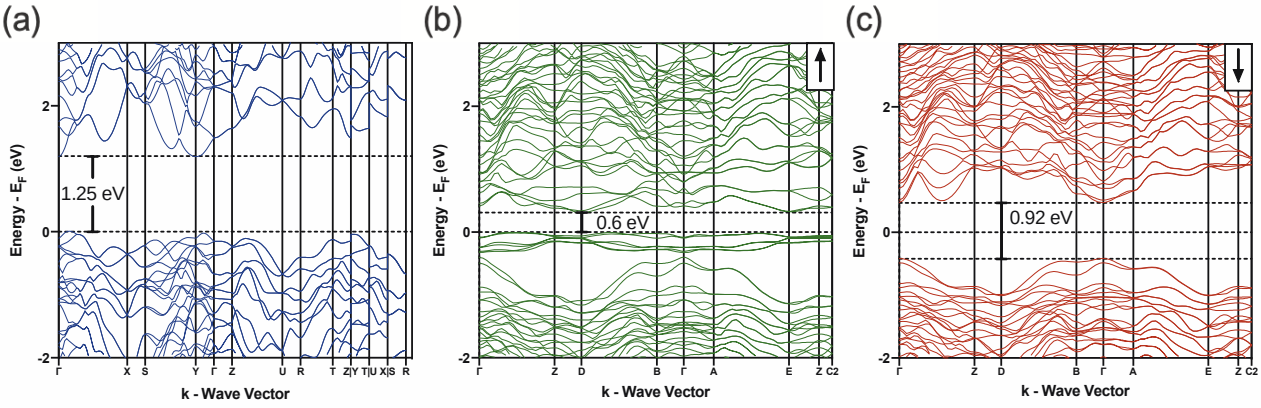

Figure 4. Electronic band structure of (a) Bi_2S_3, (b) $Bi_{23}Cr_1S_{33}Cl_3$ spin-up (↑) state, and (c) $Bi_{23}Cr_1S_{33}Cl_3$ spin-down (↓) state.

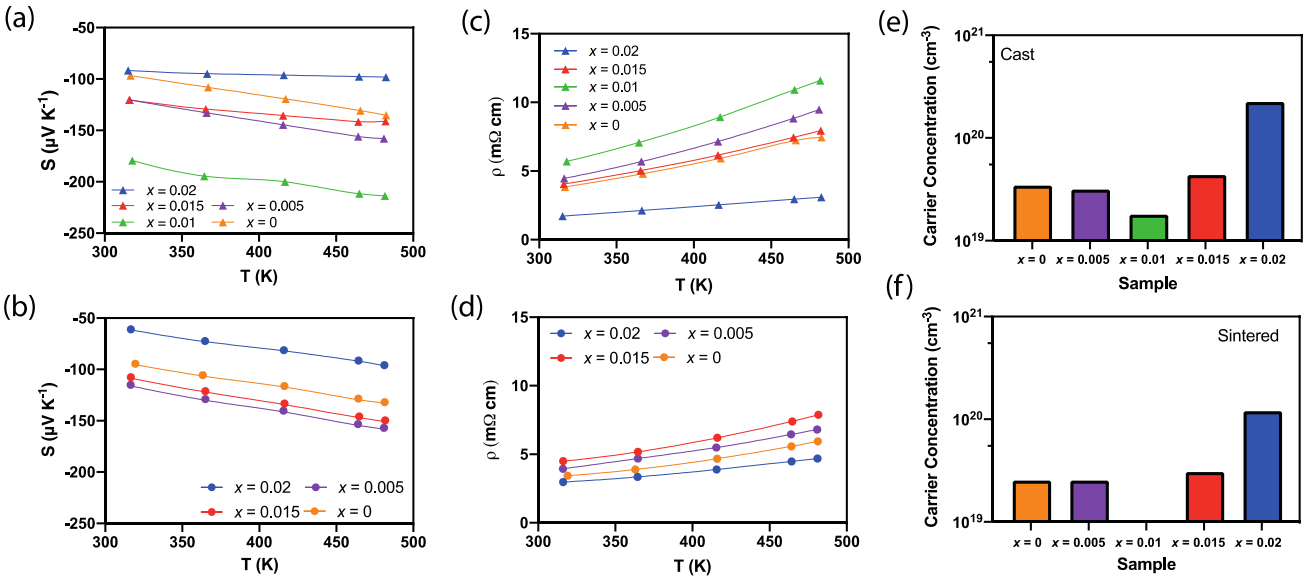

Figure 5. (a), (b) The Seebeck coefficient; (c), (d) The electrical resistivity; (e), (f) Hall carrier concentration of cast $Bi_{2-x/3}Cr_{x/3}S_{3-x}Cl_x$ (x = 0.00, 0.005, 0.01, 0.015, 0.02) and of sintered $Bi_{2-x/3}Cr_{x/3}S_{3-x}Cl_x$ (x = 0.00, 0.005, 0.015, 0.02), parallel to the direction of sintering as a function of temperature, respectively.

directions. However, the electrical resistivity of the samples parallel to the direction of sintering is slightly lower than the ones perpendicular to the sintering direction (Figure S3 of Supporting Information). The Seebeck coefficient values of sintered samples are very similar to the values obtained from ingots (Figure 5(a) and (b)), except the Seebeck coefficient of the sample with x = 0.02, for which the Seebeck coefficient reduced from ~-100 μV K^{-1} to ~-60 μV K^{-1}. Overall, the electrical resistivities of the sintered samples are lower than their cast counterparts. This is attributed to the improved mechanical integrity of sintered samples relative to the cast samples. The sintered samples with x = 0.015 and 0.02 showed a smaller reduction in resistivity compared to the ones with x = 0 and 0.005, due to the changes in the sintering conditions which made the former samples to be less dense than the latter (the sintering temperature was reduced from 723 K to 623 K for the samples with x = 0.015 and 0.02). The reproducibility of the results was verified by repeating the experiments several times (shown in Figure S5, Supporting Information).

The power factor (PF) (S^2/ρ) of the cast and sintered samples were measured parallel to the direction of sintering (Figure 6). The PF values of the doped samples are much higher than that of the pristine samples due to the optimisation of the electrical conductivity and Seebeck coefficient. The cast Bi_2S_3 sample with moderate doping (x = 0.01) exhibited the highest PF value (~566 μW m^{-1} K^{-2} at 320 K), which was about 2.3 times higher than that of the undoped Bi_2S_3 sample (about 243 μW m^{-1} K^{-2} at 320 K). The sintered sample with x = 0.01 was unavailable for measurement though. The highest power factor for the sintered sample (x = 0.005, measured along the parallel direction to the sintering pressure) was of ~367 μW m^{-1} K^{-2}at 480 K (Figure 6(b)).

The PFs obtained in this work are compared with the data reported in the literature (Figure 7). Our results are comparable with highest values reported in the literature at the same temperature.

Since, the samples in the current study have been co-doped with Cr and Cl, the relation between the measured Seebeck coefficient and carrier concentration from the cast samples are compared with previous studies of Bi_2S_3 doped with $BiCl_3$ [36], $InCl_3$ [35], $LaCl_3$ [50], $CuBr_2$ [28], and Cl [55], to illustrate the effect of doping with chromium [56] (Figure 7). The effective mass was evaluated using the single parabolic band (SPB) model with acoustic phonon scattering [57]. The model uses a Fermi integral of [58,59]:

$$F_j(\eta) = \int_0^\infty \frac{\varepsilon^j}{1 + e^{\varepsilon - \eta}} \mathrm{d}\varepsilon, \quad (1)$$

where $\eta = E_F/(k_B T)$ is the reduced Fermi level, and ε is the reduced energy of the electron state. The Seebeck and the carrier concentration are given by:

$$S = \frac{k_B}{q}\left[\frac{2F_1(\eta)}{F_0(\eta)} - \eta\right], \quad (2)$$

$$n = \frac{(2m^* k_B T)^{\frac{3}{2}}}{3\pi^2 \hbar^3} F_{1/2}(\eta), \quad (3)$$

where m^* is the effective mass.

For degenerate semiconductors, according to the Pisarenko relation [60], the Seebeck coefficient is inversely proportional to the carrier concentration, n, with a dependence of $n^{-2/3}$. The experimental data of this study deviates from this ideal relationship, which indicates the changes in the electronic band structure of the material [61]. In particular, the Seebeck coefficient values of the current study are higher than values predicted by the SPB model and experimental data of samples doped only with Cl [35,36] (as seen in Figure 8). An increase in the Seebeck at a particular carrier concentration was observed in samples

doped with La [35] (due to the presence of La nanoprecipitates) and $CuBr_2$ (due to the energy filtering effect [62]). It is worth noting that although Cu is not a magnetic element, it interacts with magnets.

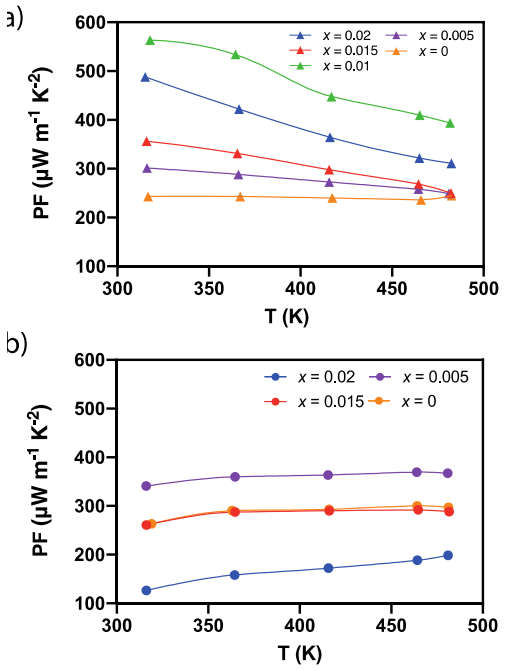

Figure 6. (a), (b) The power factor of cast $Bi_{2-x/3}Cr_{x/3}S_{3-x}Cl_x$ (x = 0.00, 0.005, 0.01, 0.015, 0.02) and of sintered $Bi_{2-x/3}Cr_{x/3}S_{3-x}Cl_x$ (x = 0.00, 0.005, 0.015, 0.02) along the parallel direction of the sintering pressure as a function of temperature, respectively.

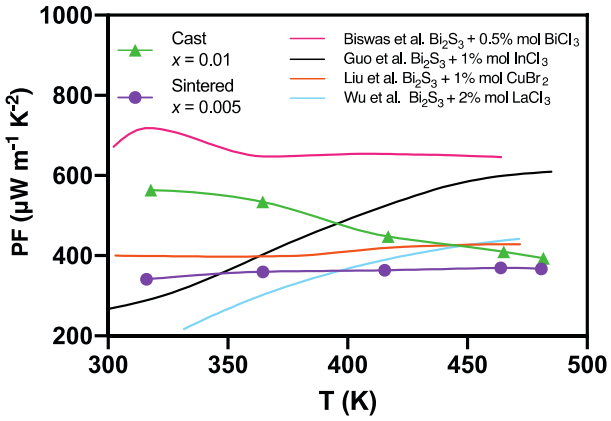

Figure 7. Power factor comparison of n-type Bi_2S_3 doped with 0.5% mol $BiCl_3$ [36], 2% mol $InCl_3$ [35], 2% $LaCl_3$ [50], and 1% $CuBr_2$ [28] with sintered $Bi_{2-x/3}Cr_{x/3}S_{3-x}Cl_x$ (x = 0.005) and cast $Bi_{2-x/3}Cr_{x/3}S_{3-x}Cl_x$ (x = 0.01) as a function of temperature.

The higher values of the Seebeck coefficient obtained in the current study, might be attributed to a magnetic drag effect generated by the magnetic chromium dopant [18–23]. It has been shown for example in the case of magnetic materials that an additional contribution to the Seebeck coefficient is observed when the materials are subjected to a temperature gradient, due to the flux of magnons [63,64]. The interaction between magnons and carriers results in an overall increase in the effective mass and consequently, in the Seebeck coefficient [65]. Similar Seebeck enhancement effects have been observed for nonmagnetic materials doped with magnetic elements, similar to the present case [18,19,21,24]. In the present study, the effective mass of the cast samples increased significantly from $0.7m_0$ for the pristine sample to $2.1m_0$ for the sample with x = 0.02 (Table 1), where m_0 is the electron rest mass. This enhanced mass contributed to the higher Seebeck coefficient compared with materials doped only with Cl [36,55], and it supports the hypothesis of carriers interactions with magnetic elements. The carrier mobilities also decreased with the increase in the concentration of Chromium (Table 1). The reduction of charge carrier mobility is responsible for a decrease in the electrical conductivity [66,67]. However, the overall effect was an increase in the power factor for the lightly doped sample given the enhanced Seebeck coefficient due to the increased effective mass.

For the sintered samples, the measured carrier concentrations were 2.54×10^{19}, 2.56×10^{19}, 3.08×10^{19}, 1.2×10^{20} cm^{-3} and mobilities were 60.4, 47.8, 40, 53.3 $cm^2\ V^{-1}\ s^{-1}$ for sintered $Bi_{2-x/3}Cr_{x/3}S_{3-x}Cl_x$ (x = 0.00, 0.005, 0.015, 0.02), respectively.

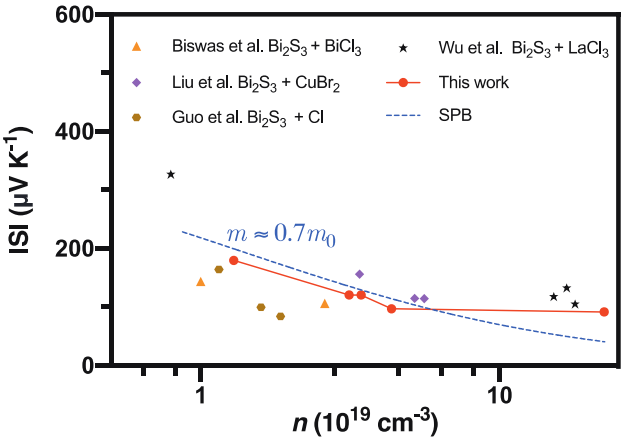

Figure 8. Hall carrier concentration dependence of room temperature Seebeck coefficient of n-type cast $Bi_{2-x/3}Cr_{x/3}S_{3-x}Cl_x$ compared to those reported in the literature of Bi_2S_3 doped $BiCl_3$ [13], $LaCl_3$ [35], $CuBr_2$ [5], and Cl [40].

Table 1. Carrier Concentration, mobility, and calculated effective mass cast $Bi_{2-x/3}Cr_{x/3}S_{3-x}Cl_x$

Sample ($Bi_{2-x/3}Cr_{x/3}S_{3-x}Cl_x$)	n ($\times 10^{19}$ cm^{-3})	μ ($cm^2\ V^{-1}\ s^{-1}$)	m^*/m_0
x = 0	3.44	15.1	0.76
x = 0.005	3.14	28.2	0.79
x = 0.01	1.79	24.5	0.83
x = 0.015	4.35	16.7	0.75
x = 0.02	22.4	7.59	2.10

The temperature dependence of κ_{total}, κ_e and κ_L for sintered $Bi_{2-x/3}Cr_{x/3}S_{3-x}Cl_x$ (x = 0.00, 0.005, 0.015, 0.02) samples measured parallel to the direction of sintering are presented in Figure 9. The total thermal conductivity is the sum of the electronic and lattice thermal conductivity $\kappa_L = \kappa_{total} - \kappa_e$.

The electronic thermal conductivity, κ_e, was obtained using the Wiedemann-Franz law, which is expressed as $\kappa_e = L\sigma T$. The Lorenz number (L) values as a function of temperature were estimated from the SPB model (Figure S4 of supporting Information) [57]:

$$L = \left(\frac{k_B}{q}\right)^2 \left[\frac{3F_0(\eta)F_2(\eta) - 4F_1^2(\eta)}{F_0^2(\eta)}\right]. \quad (4)$$

The values of the electronic thermal conductivity (Figure 9(b)) are larger for the doped samples given their higher carrier concentrations (Figure 5(f)). The values of the lattice thermal conductivity for all samples are very close to the values of κ_{total} (Figures 8(c) and (a)), due to a small contribution of electronic thermal conductivity to the total thermal conductivity of Bi_2S_3. The κ_{total} values of all the samples ranged from ~0.8 to ~1.1 W m^{-1} K^{-1} at 320 K and ranged from ~0.6 to ~0.8 W m^{-1} K^{-1} at 480 K (Figure 9(a)). The samples that were sintered at the lower temperature of 673 K (x = 0.015 and x = 0.02) have larger thermal conductivity. Nevertheless, all samples have similar values of lattice thermal conductivity (Figure 9(c)). The reproducibility of the thermal diffusivity results was verified by repeating the experiment several times, the results are shown in the Figure S6, Supporting Information.
To further study this and the effect of the dopant on the scattering mechanism of phonons in these samples, the Debye–Callaway model was adopted to evaluate the thermal conductivity [68,69]:

$$\kappa_L = \frac{k_b}{2\pi^2 v_s}\left(\frac{k_b T}{\hbar}\right)^3 \int_0^{\frac{\theta_D}{T}} \frac{x^4 e^x}{\tau_C^{-1}(e^x - 1)^2}\mathrm{d}x, \quad (5)$$

where $x = \hbar\omega/k_B T$ is the reduced frequency, ω the phonon angular frequency, k_B the Boltzmann constant, v_s the speed of sound, $\hbar$ the reduced Planck constant, θ_D the Debye temperature, and τ_C the combined phonon relaxation time. The values of $\theta_D = 283$ K and $v_s = 2775$ m s^{-1} were adopted from the literature [70].
Four mechanisms of phonon scattering were considered: point impurities, normal three-phonon process, Umklapp process, and boundary scattering [71]. Matthiessen's rule [72] is employed to find the combined phonon relaxation time:

$$\tau_C^{-1} = \tau_I^{-1} + \tau_N^{-1} + \tau_U^{-1} + \tau_B^{-1} = A\omega^4 + \beta\tau_U^{-1} + B_U T\omega^2 e^{-\frac{\theta_D}{3T}} + \frac{v_s}{L}, \quad (6)$$

where τ_I, τ_N, τ_U and τ_B are, respectively, the relaxation times for points impurities scattering, normal three phonon process, Umklapp process, and boundary scattering, L is the average
grain size, and the coefficients A, β, B_U are fitting parameters. Table 2 presents the calculated parameters for all sintered samples parallel to the direction of sintering. The average grain size was obtained from the Rietveld refinement of XRD patterns obtained from samples. The fitted values are shown by dashed lines in Figure 9(c).

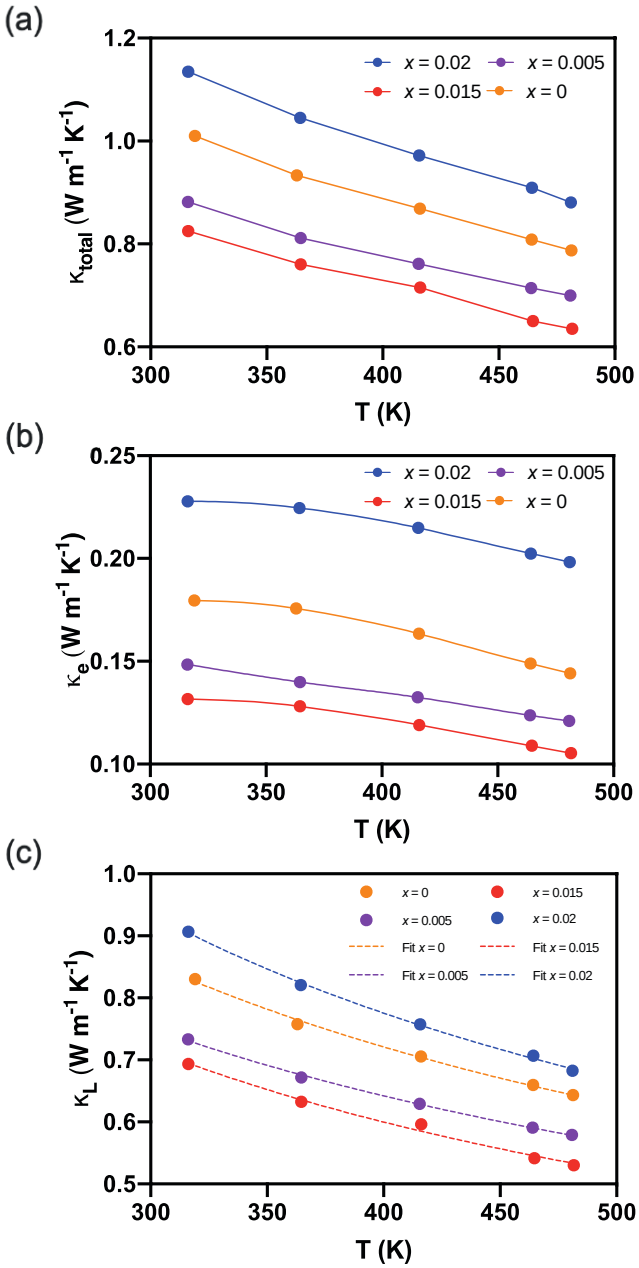

Figure 9. (a) The total thermal conductivity; (b) the electronic thermal conductivity; (c) and the lattice thermal conductivity (the dashed lines are the calculations based on the Debye–Callaway model) of sintered $Bi_{2-x/3}Cr_{x/3}S_{3-x}Cl_x$ (x = 0.00, 0.005, 0.015, 0.02) parallel to the direction of sintering as a function of temperature.

Table 2. Calculated Parameters for the Debye–Callaway Model for sintered $Bi_{2-x/3}Cr_{x/3}S_{3-x}Cl_x$ (x = 0.00, 0.005, 0.015, 0.02) samples parallel to the direction of sintering

x	A ($\times 10^{-41}$ s^3)	β	B_U ($\times 10^{-18}$ s K)	L (μm)
0	4.9	2.2	3.6	1.3
0.005	7.3	6.3	1.4	1.4
0.015	5.6	6.4	2.0	1.3
0.02	3.5	2.4	3.9	1.5

The results show a noticeable increase in the scattering by point defects with increasing dopant concentration. In general, the thermal conductivity values of the sintered samples are similar for all samples. The changes in β and B_U indicates that the main mechanism caused these differences was due to changes in the phonon-phonon scattering.

Figure 10 shows the *z*T values for the sintered samples (measured parallel to the direction of sintering). The maximum *z*T value of ~0.25 was achieved for the sample with $x = 0.005$ at 480 K. It is worth noting that the sample $Bi_{2-x/3}Cr_{x/3}S_{3-x}Cl_x$ ($x = 0.01$) with potentially highest *z*T value was unavailable in the sintered form for measurement. Figure 10(b) compares the *z*T values of the samples in the current study samples with the largest values reported in literature at the same temperature. There is a difference in the *z*T values obtained from measurements performed parallel and perpendicular to the direction of sintering, due to crystal structure of Bi_2S_3 (Figure S3 of Supporting Information).

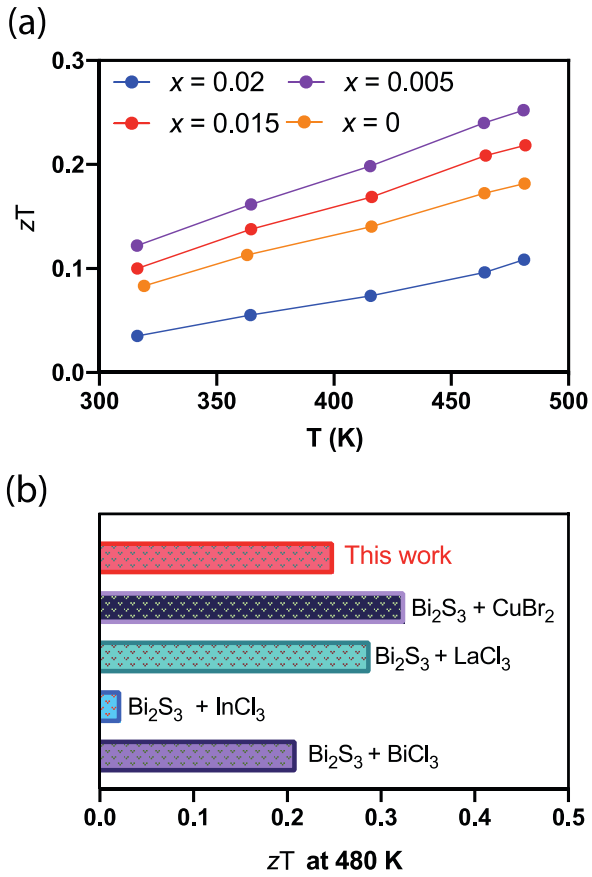

Figure 10. (a) *z*T values of sintered $Bi_{2-x/3}Cr_{x/3}S_{3-x}Cl_x$ (x = 0.00, 0.005, 0.015, 0.02) parallel to the direction of sintering as a function of temperature; (b) *z*T of sintered $Bi_{2-x/3}Cr_{x/3}S_{3-x}Cl_x$ ($x = 0.005$) at 480 K compared to $BiCl_3$ [36], 2% mol $InCl_3$ [35], 2% $LaCl_3$ [50], and 1% $CuBr_2$ [28].

CONCLUSIONS

Bi_2S_3 was successfully doped with $CrCl_3$ using the melting-annealing technique followed by sintering by the SPS. The electronic properties were measured for both the cast and sintered samples. Compared to samples with non-magnetic dopants, the Seebeck coefficient increased at the same carrier concentration, which was most likely due to the magnon drag effect, where the interaction between magnons and carriers effectively increases the effective mass of the carriers and consequently the Seebeck coefficient. The increase in the effective mass led to a decrease in the carrier mobility and the electrical conductivity of the samples with higher carrier concentration. Thermal conductivity measurements of the sintered samples showed similar values for all the samples, with differences arising from the carrier concentration and increased scattering due to impurities. The *z*T values of this work are comparable to the largest values reported in literature and provided experimental evidence that the presence of magnetic dopants can increase the overall efficiency of thermoelectric materials.

ASSOCIATED CONTENT

Supporting Information

Measured density of the samples; Powder diffraction pattern and refined lattice parameters of sintered samples; Transport properties and figure of merit of samples, perpendicular to the direction of sintering; Heat capacity and Lorenz number used in the thermal conductivity calculations; Additional measurements for the transport properties; Error analysis for the Seebeck coefficient and resistivity.

AUTHOR CONTRIBUTIONS

The manuscript was written through contributions of all authors. All authors have given approval to the final version of the manuscript.

ACKNOWLEDGMENT

The project has received funding from the European Union's Horizon 2020 research and innovation programme under the Marie Skłodowska-Curie grant agreement No. 801604. T.M. would like to thank JST Mirai Program JPMJMI19A1 for support.

REFERENCES

(1) Delaire, O.; Ma, J.; Marty, K.; May, A. F.; McGuire, M. A.; Du, M. H.; Singh, D. J.; Podlesnyak, A.; Ehlers, G.; Lumsden, M. D.; Sales, B. C. Giant Anharmonic Phonon Scattering in PbTe. *Nature Mater* **2011**, *10* (8), 614–619. https://doi.org/10.1038/nmat3035.

(2) Hu, Y.; Zeng, L.; Minnich, A. J.; Dresselhaus, M. S.; Chen, G. Spectral Mapping of Thermal Conductivity through Nanoscale Ballistic Transport. *Nat Nanotechnol* **2015**, *10* (8), 701–706. https://doi.org/10.1038/nnano.2015.109.

(3) Hu, L.; Zhang, Y.; Wu, H.; Li, J.; Li, Y.; McKenna, M.; He, J.; Liu, F.; Pennycook, S. J.; Zeng, X. Entropy Engineering of SnTe: Multi-Principal-Element Alloying Leading to Ultralow Lattice Thermal Conductivity and State-of-the-Art Thermoelectric Performance. *Advanced Energy Materials* **2018**, *8* (29), 1802116. https://doi.org/10.1002/aenm.201802116.

(4) Wei, P. C.; Liao, C. N.; Wu, H. J.; Yang, D.; He, J.; Biesold-McGee, G. V.; Liang, S.; Yen, W. T.; Tang, X.; Yeh, J. W.; Lin, Z.; He, J. H. Thermodynamic

Routes to Ultralow Thermal Conductivity and High Thermoelectric Performance. *Adv Mater* **2020**, *32* (12), e1906457. https://doi.org/10.1002/adma.201906457.

(5) Joshi, G.; Lee, H.; Lan, Y.; Wang, X.; Zhu, G.; Wang, D.; Gould, R. W.; Cuff, D. C.; Tang, M. Y.; Dresselhaus, M. S.; Chen, G.; Ren, Z. Enhanced Thermoelectric Figure-of-Merit in Nanostructured p-Type Silicon Germanium Bulk Alloys. *Nano Lett.* **2008**, *8* (12), 4670–4674. https://doi.org/10.1021/nl8026795.

(6) Lan, Y. C.; Minnich, A. J.; Chen, G.; Ren, Z. F. Enhancement of Thermoelectric Figure-of-Merit by a Bulk Nanostructuring Approach. *Adv Funct Mater* **2010**, *20* (3), 357–376. https://doi.org/10.1002/adfm.200901512.

(7) Wang, H.; Cao, X.; Takagiwa, Y.; Snyder, G. J. Higher Mobility in Bulk Semiconductors by Separating the Dopants from the Charge-Conducting Band – a Case Study of Thermoelectric PbSe. *Materials Horizons* **2015**, *2* (3), 323–329. https://doi.org/10.1039/c5mh00021a.

(8) Yu, B.; Zebarjadi, M.; Wang, H.; Lukas, K.; Wang, H.; Wang, D.; Opeil, C.; Dresselhaus, M.; Chen, G.; Ren, Z. Enhancement of Thermoelectric Properties by Modulation-Doping in Silicon Germanium Alloy Nanocomposites. *Nano Lett* **2012**, *12* (4), 2077–2082. https://doi.org/10.1021/nl3003045.

(9) Heremans, J. P.; Jovovic, V.; Toberer, E. S.; Saramat, A.; Kurosaki, K.; Charoenphakdee, A.; Yamanaka, S.; Snyder, G. J. Enhancement of Thermoelectric Efficiency in PbTe by Distortion of the Electronic Density of States. *Science*, 2008, *321*, 554–557. https://doi.org/10.1126/science.1159725.

(10) Rhyee, J. S.; Lee, K. H.; Lee, S. M.; Cho, E.; Kim, S. I.; Lee, E.; Kwon, Y. S.; Shim, J. H.; Kotliar, G. Peierls Distortion as a Route to High Thermoelectric Performance in In(4)Se(3-Delta) Crystals. *Nature* **2009**, *459* (7249), 965–968. https://doi.org/10.1038/nature08088.

(11) Zhou, J.; Yang, R.; Chen, G.; Dresselhaus, M. S. Optimal Bandwidth for High Efficiency Thermoelectrics. *Phys. Rev. Lett.* **2011**, *107* (22), 226601. https://doi.org/10.1103/PhysRevLett.107.226601.

(12) Zeng, G.; Bowers, J. E.; Zide, J. M. O.; Gossard, A. C.; Kim, W.; Singer, S.; Majumdar, A.; Singh, R.; Bian, Z.; Zhang, Y.; Shakouri, A. ErAs:InGaAs/InGaAlAs Superlattice Thin-Film Power Generator Array. *Appl. Phys. Lett.* **2006**, *88* (11), 113502. https://doi.org/10.1063/1.2186387.

(13) Gu, Y.; Ai, W.; Zhao, Y.; Pan, L.; Lu, C.; Zong, P.; Hu, X.; Xu, Z.; Wang, Y. Remarkable Thermoelectric Property Enhancement in Cu2SnS3–CuCo2S4 Nanocomposites via 3D Modulation Doping. *J. Mater. Chem. A* **2021**, *9* (31), 16928–16935. https://doi.org/10.1039/D1TA02812J.

(14) Hou, Q. R.; Gu, B. F.; Chen, Y. B.; He, Y. J.; Sun, J. L. Enhancement of the Thermoelectric Power Factor of MnSi1.7 Film by Modulation Doping of Al and Cu. *Appl Phys a-Mater* **2014**, *114* (3), 943–949. https://doi.org/10.1007/s00339-013-7794-0.

(15) Zebarjadi, M.; Joshi, G.; Zhu, G.; Yu, B.; Minnich, A.; Lan, Y.; Wang, X.; Dresselhaus, M.; Ren, Z.; Chen, G. Power Factor Enhancement by Modulation Doping in Bulk Nanocomposites. *Nano Lett* **2011**, *11* (6), 2225–2230. https://doi.org/10.1021/nl201206d.

(16) Kim, R.; Lundstrom, M. S. Computational Study of Energy Filtering Effects in One-Dimensional Composite Nano-Structures. *J Appl Phys* **2012**, *111* (2), 024508. https://doi.org/10.1063/1.3678001.

(17) Cho, H.; Back, S. Y.; Yun, J. H.; Byeon, S.; Jin, H.; Rhyee, J. S. Thermoelectric Properties and Low-Energy Carrier Filtering by Mo Microparticle Dispersion in an n-Type (CuI)0.003Bi2(Te,Se)3 Bulk Matrix. *ACS Appl Mater Interfaces* **2020**, *12* (34), 38076–38084. https://doi.org/10.1021/acsami.0c09529.

(18) Ahmed, F.; Tsujii, N.; Mori, T. Thermoelectric Properties of CuGa1−xMnxTe2: Power Factor Enhancement by Incorporation of Magnetic Ions. *Journal of Materials Chemistry A* **2017**, *5* (16), 7545–7554. https://doi.org/10.1039/c6ta11120c.

(19) Acharya, S.; Anwar, S.; Mori, T.; Soni, A. Coupling of Charge Carriers with Magnetic Entropy for Power Factor Enhancement in Mn Doped Sn1.03Te for Thermoelectric Applications. *Journal of Materials Chemistry C* **2018**, *6* (24), 6489–6493. https://doi.org/10.1039/c8tc00788h.

(20) Takaki, H.; Kobayashi, K.; Shimono, M.; Kobayashi, N.; Hirose, K.; Tsujii, N.; Mori, T. Thermoelectric Properties of a Magnetic Semiconductor CuFeS2. *Materials Today Physics* **2017**, *3*, 85–92. https://doi.org/10.1016/j.mtphys.2017.12.006.

(21) Mori, T. Novel Principles and Nanostructuring Methods for Enhanced Thermoelectrics. *Small* **2017**, *13* (45), 1–10. https://doi.org/10.1002/smll.201702013.

(22) Tsujii, N.; Mori, T. High Thermoelectric Power Factor in a Carrier-Doped Magnetic Semiconductor Cufes2. *Applied Physics Express* **2013**, *6* (4), 043001. https://doi.org/10.7567/APEX.6.043001.

(23) Tsujii, N.; Nishide, A.; Hayakawa, J.; Mori, T. Observation of Enhanced Thermopower Due to Spin Fluctuation in Weak Itinerant Ferromagnet. *Science Advances 5* (2), eaat5935. https://doi.org/10.1126/sciadv.aat5935.

(24) Vaney, J. B.; Yamini, S. A.; Takaki, H.; Kobayashi, K.; Kobayashi, N.; Mori, T. Magnetism-Mediated Thermoelectric Performance of the Cr-Doped Bismuth Telluride Tetradymite. *Mater Today Phys* **2019**, *9*, 100090. https://doi.org/10.1016/j.mtphys.2019.03.004.

(25) Liu, W.; Lukas, K. C.; McEnaney, K.; Lee, S.; Zhang, Q.; Opeil, C. P.; Chen, G.; Ren, Z. Studies on the Bi2Te3-Bi2Se 3-Bi2S3 System for Mid-Temperature Thermoelectric Energy Conversion. *Energy and Environmental Science* **2013**, *6* (2), 552–560. https://doi.org/10.1039/c2ee23549h.

(26) Guo, Y.; Du, X.; Wang, Y.; Yuan, Z. Simultaneous Enhanced Performance of Electrical Conductivity and Seebeck Coefficient in Bi2−Sn S3 by Solvothermal and Microwave Sintering. *Journal of Alloys and Compounds* **2017**, *717*, 177–182. https://doi.org/10.1016/j.jallcom.2017.05.067.

(27) Chen, B.; Uher, C.; Iordanidis, L.; Kanatzidis, M. G. Transport Properties of Bi2S3and the Ternary Bismuth Sulfides KBi6.33S10and K2Bi8S13. *Chem Mater* **1997**, *9* (7), 1655–1658. https://doi.org/10.1021/cm970033m.

(28) Liu, Z. H.; Pei, Y. L.; Geng, H. Y.; Zhou, J. C.; Meng, X. F.; Cai, W.; Liu, W. S.; Sui, J. H. Enhanced Thermoelectric Performance of Bi2S3 by Synergistical Action of Bromine Substitution and Copper Nanoparticles. *Nano Energy* **2015**, *13*, 554–562. https://doi.org/10.1016/j.nanoen.2015.03.036.

(29) Kawamoto, Y.; Iwasaki, H. Thermoelectric Properties of (Bi1−x Sb x)2S3 with Orthorhombic Structure.

Journal of Elec Materi **2014**, *43* (6), 1475–1479. https://doi.org/10.1007/s11664-013-2742-5.

(30) Ge, Z. H.; Zhang, B. P.; Liu, Y.; Li, J. F. Nanostructured Bi(2-x)Cu(x)S3 Bulk Materials with Enhanced Thermoelectric Performance. *Phys. Chem. Chem. Phys.* **2012**, *14* (13), 4475–4481. https://doi.org/10.1039/c2cp23955h.

(31) Yu, Y. Q.; Zhang, B. P.; Ge, Z. H.; Shang, P. P.; Chen, Y. X. Thermoelectric Properties of Ag-Doped Bismuth Sulfide Polycrystals Prepared by Mechanical Alloying and Spark Plasma Sintering. *Mater Chem Phys* **2011**, *131* (1–2), 216–222. https://doi.org/10.1016/j.matchemphys.2011.09.010.

(32) Yang, J.; Liu, G. W.; Yan, J. N.; Zhang, X. Z.; Shi, Z. Q.; Qiao, G. J. Enhanced the Thermoelectric Properties of N-Type Bi2S3 Polycrystalline by Iodine Doping. *J Alloy Compd* **2017**, *728*, 351–356. https://doi.org/10.1016/j.jallcom.2017.08.148.

(33) Du, X. L.; Cai, F. S.; Wang, X. W. Enhanced Thermoelectric Performance of Chloride Doped Bismuth Sulfide Prepared by Mechanical Alloying and Spark Plasma Sintering. *J Alloy Compd* **2014**, *587*, 6–9. https://doi.org/10.1016/j.jallcom.2013.10.185.

(34) Chen, Y.; Wang, D.; Zhou, Y.; Pang, Q.; Shao, J.; Wang, G.; Wang, J.; Zhao, L.-D. Enhancing the Thermoelectric Performance of Bi2S3: A Promising Earth-Abundant Thermoelectric Material. *Front Phys-Beijing* **2018**, *14* (1), 13. https://doi.org/10.1007/s11467-018-0845-4.

(35) Guo, J.; Ge, Z. H.; Qian, F.; Lu, D. H.; Feng, J. Achieving High Thermoelectric Properties of Bi2S3 via InCl3 Doping. *J Mater Sci* **2020**, *55* (1), 263–273. https://doi.org/10.1007/s10853-019-04008-3.

(36) Biswas, K.; Zhao, L. D.; Kanatzidis, M. G. Tellurium-Free Thermoelectric: The Anisotropic n-Type Semiconductor Bi2S3. *Adv Energy Mater* **2012**, *2* (6), 634–638. https://doi.org/10.1002/aenm.201100775.

(37) Wang, Z. Y.; Guo, J.; Feng, J.; Ge, Z. H. Effects of NbCl5-Doping on the Thermoelectric Properties of Polycrystalline Bi2S3. *J Solid State Chem* **2021**, *297*, 122043. https://doi.org/10.1016/j.jssc.2021.122043.

(38) Zhang, L. J.; Zhang, B. P.; Ge, Z. H.; Han, C. G. Fabrication and Properties of Bi2S3-XSex Thermoelectric Polycrystals. *Solid State Commun* **2013**, *162*, 48–52. https://doi.org/10.1016/j.ssc.2013.03.013.

(39) Ge, Z. H.; Zhang, B. P.; Shang, P. P.; Li, J. F. Control of Anisotropic Electrical Transport Property of Bi2S3 Thermoelectric Polycrystals. *J Mater Chem* **2011**, *21* (25), 9194–9200. https://doi.org/10.1039/c1jm11069a.

(40) Ge, Z.-H.; Zhang, B.-P.; Li, J.-F. Microstructure Composite-like Bi2S3 Polycrystals with Enhanced Thermoelectric Properties. *J. Mater. Chem.* **2012**, *22* (34), 17589. https://doi.org/10.1039/c2jm33603k.

(41) Zhao, L. D.; Zhang, B. P.; Liu, W. S.; Zhang, H. L.; Li, J. F. Enhanced Thermoelectric Properties of Bismuth Sulfide Polycrystals Prepared by Mechanical Alloying and Spark Plasma Sintering. *J Solid State Chem* **2008**, *181* (12), 3278–3282. https://doi.org/10.1016/j.jssc.2008.08.022.

(42) Guo, J.; Zhang, Y. X.; Wang, Z. Y.; Zheng, F. S.; Ge, Z. H.; Fu, J. C.; Feng, J. High Thermoelectric Properties Realized in Earth-Abundant Bi2S3 Bulk via Carrier Modulation and Multi-Nano-Precipitates Synergy. *Nano Energy* **2020**, *78*, 105227. https://doi.org/10.1016/j.nanoen.2020.105227.

(43) Toby, B. H.; Von Dreele, R. B. GSAS-II : The Genesis of a Modern Open-Source All Purpose Crystallography Software Package. *Journal of Applied Crystallography* **2013**, *46* (2), 544–549. https://doi.org/10.1107/S0021889813003531.

(44) Perdew, J. P.; Burke, K.; Ernzerhof, M. Generalized Gradient Approximation Made Simple. *Phys. Rev. Lett.* **1996**, *77* (18), 3865–3868. https://doi.org/10.1103/PhysRevLett.77.3865.

(45) Giannozzi, P.; Baseggio, O.; Bonfà, P.; Brunato, D.; Car, R.; Carnimeo, I.; Cavazzoni, C.; de Gironcoli, S.; Delugas, P.; Ferrari Ruffino, F.; Ferretti, A.; Marzari, N.; Timrov, I.; Urru, A.; Baroni, S. Quantum ESPRESSO toward the Exascale. *J. Chem. Phys.* **2020**, *152* (15), 154105. https://doi.org/10.1063/5.0005082.

(46) Monkhorst, H. J.; Pack, J. D. Special Points for Brillouin-Zone Integrations. *Phys. Rev. B* **1976**, *13* (12), 5188–5192. https://doi.org/10.1103/PhysRevB.13.5188.

(47) Pauling, L. *The Nature of the Chemical Bond and the Structure of Molecules and Crystals: An Introduction to Modern Structural Chemistry*, Third.; Cornell University Press, 1960.

(48) Lundegaard, L. F.; Makovicky, E. E.; Boffa-Ballaran, T.; Balic-Zunic, T. Crystal Structure and Cation Lone Electron Pair Activity of Bi2S3 between 0 and 10 GPa. *Phys Chem Miner* **2005**, *32* (8–9), 578–584. https://doi.org/10.1007/s00269-005-0033-2.

(49) Ji, W.; Shi, X.-L.; Liu, W.-D.; Yuan, H.; Zheng, K.; Wan, B.; Shen, W.; Zhang, Z.; Fang, C.; Wang, Q.; Chen, L.; Zhang, Y.; Jia, X.; Chen, Z.-G. Boosting the Thermoelectric Performance of N-Type Bi2S3 by Hierarchical Structure Manipulation and Carrier Density Optimization. *Nano Energy* **2021**, *87*, 106171. https://doi.org/10.1016/j.nanoen.2021.106171.

(50) Wu, Y.; Lou, Q.; Qiu, Y.; Guo, J.; Mei, Z. Y.; Xu, X.; Feng, J.; He, J. Q.; Ge, Z. H. Highly Enhanced Thermoelectric Properties of Nanostructured Bi2S3 Bulk Materials via Carrier Modification and Multi-Scale Phonon Scattering. *Inorg Chem Front* **2019**, *6* (6), 1374–1381. https://doi.org/10.1039/c9qi00213h.

(51) Jonson, M.; Mahan, G. D. Mott's Formula for the Thermopower and the Wiedemann-Franz Law. *Physical Review B* **1980**, *21* (10), 4223–4229. https://doi.org/10.1103/PhysRevB.21.4223.

(52) Guo, J.; Lou, Q.; Qiu, Y.; Wang, Z.-Y.; Ge, Z.-H.; Feng, J.; He, J. Remarkably Enhanced Thermoelectric Properties of Bi2S3 Nanocomposites via Modulation Doping and Grain Boundary Engineering. *Applied Surface Science* **2020**, *520*, 146341. https://doi.org/10.1016/j.apsusc.2020.146341.

(53) Tan, X. F.; Tan, X. J.; Liu, G. Q.; Xu, J. T.; Shao, H. Z.; Hu, H. Y.; Jin, M.; Jiang, H. C.; Jiang, J. Optimizing the Thermoelectric Performance of In-Cd Codoped SnTe by Introducing Sn Vacancies. *J Mater Chem C* **2017**, *5* (30), 7504–7509. https://doi.org/10.1039/c7tc02162c.

(54) Chen, S.; Bai, H.; Li, J.; Pan, W.; Jiang, X.; Li, Z.; Chen, Z.; Yan, Y.; Su, X.; Wu, J.; Uher, C.; Tang, X. Vacancy-Based Defect Regulation for High Thermoelectric Performance in Ge9Sb2Te12-x Compounds. *ACS Appl. Mater. Interfaces* **2020**, *12* (17), 19664–19673. https://doi.org/10.1021/acsami.0c02155.

(55) Guo, J.; Yang, J.; Ge, Z.-H.; Jiang, B.; Qiu, Y.; Zhu, Y.-K.; Wang, X.; Rong, J.; Yu, X.; Feng, J.; He, J. Realizing High Thermoelectric Performance in Earth-

Abundant Bi2S3 Bulk Materials via Halogen Acid Modulation. *Advanced Functional Materials* **2021**, *31* (37), 2102838. https://doi.org/10.1002/adfm.202102838.

(56) Kang, S. D.; Snyder, G. J. Transport Property Analysis Method for Thermoelectric Materials: Material Quality Factor and the Effective Mass Model. *arXiv:1710.06896 [cond-mat]* **2018**.

(57) May, A. F.; Snyder, G. J. Introduction to Modeling Thermoelectric Transport at High Temperatures. In *Materials, Preparation, and Characterization in Thermoelectrics*; CRC Press, 2012.

(58) Pei, Y. Z.; LaLonde, A. D.; Wang, H.; Snyder, G. J. Low Effective Mass Leading to High Thermoelectric Performance. *Energ Environ Sci* **2012**, *5* (7), 7963–7969. https://doi.org/10.1039/c2ee21536e.

(59) Naithani, H.; Dasgupta, T. Critical Analysis of Single Band Modeling of Thermoelectric Materials. *ACS Appl. Energy Mater.* **2020**, *3* (3), 2200–2213. https://doi.org/10.1021/acsaem.9b02015.

(60) Ravich, Iu. I. *Semiconducting Lead Chalcogenides*; Monographs in Semiconductor Physics; Springer US, 1970. https://doi.org/10.1007/978-1-4684-8607-0.

(61) Zou, T.; Qin, X.; Zhang, Y.; Li, X.; Zeng, Z.; Li, D.; Zhang, J.; Xin, H.; Xie, W.; Weidenkaff, A. Enhanced Thermoelectric Performance of β-Zn4Sb3 Based Nanocomposites through Combined Effects of Density of States Resonance and Carrier Energy Filtering. *Sci Rep* **2015**, *5* (1), 17803. https://doi.org/10.1038/srep17803.

(62) Liu, M.; Qin, X. Y. Enhanced Thermoelectric Performance through Energy-Filtering Effects in Nanocomposites Dispersed with Metallic Particles. *Appl Phys Lett* **2012**, *101* (13), 132103. https://doi.org/10.1063/1.4755768.

(63) Costache, M. V.; Bridoux, G.; Neumann, I.; Valenzuela, S. O. Magnon-Drag Thermopile. *Nat Mater* **2011**, *11* (3), 199–202. https://doi.org/10.1038/nmat3201.

(64) Watzman, S. J.; Duine, R. A.; Tserkovnyak, Y.; Boona, S. R.; Jin, H.; Prakash, A.; Zheng, Y. H.; Heremans, J. P. Magnon-Drag Thermopower and Nernst Coefficient in Fe, Co, and Ni. *Phys Rev B* **2016**, *94* (14), 144407. https://doi.org/10.1103/PhysRevB.94.144407.

(65) Ang, R.; Khan, A. U.; Tsujii, N.; Takai, K.; Nakamura, R.; Mori, T. Thermoelectricity Generation and Electron-Magnon Scattering in a Natural Chalcopyrite Mineral from a Deep-Sea Hydrothermal Vent. *Angew Chem Int Ed Engl* **2015**, *54* (44), 12909–12913. https://doi.org/10.1002/anie.201505517.

(66) Ge, B.; Shi, Z.; Zhou, C.; Hu, J.; Liu, G.; Xia, H.; Xu, J.; Qiao, G. Enhanced Thermoelectric Performance of N-Type Eco-Friendly Material Cu1-XAgxFeS2 (X=0–0.14) via Bandgap Tuning. *Journal of Alloys and Compounds* **2019**, *809*, 151717. https://doi.org/10.1016/j.jallcom.2019.151717.

(67) Xiao, Y.; Wang, D.; Zhang, Y.; Chen, C.; Zhang, S.; Wang, K.; Wang, G.; Pennycook, S. J.; Snyder, G. J.; Wu, H.; Zhao, L.-D. Band Sharpening and Band Alignment Enable High Quality Factor to Enhance Thermoelectric Performance in n -Type PbS. *J. Am. Chem. Soc.* **2020**, *142* (8), 4051–4060. https://doi.org/10.1021/jacs.0c00306.

(68) He, J.; Girard, S. N.; Kanatzidis, M. G.; Dravid, V. P. Microstructure-Lattice Thermal Conductivity Correlation in Nanostructured PbTe0.7S0.3 Thermoelectric Materials. *Advanced Functional Materials* **2010**, *20* (5), 764–772. https://doi.org/10.1002/adfm.200901905.

(69) Callaway, J. Model for Lattice Thermal Conductivity at Low Temperatures. *Phys. Rev.* **1959**, *113* (4), 1046–1051. https://doi.org/10.1103/PhysRev.113.1046.

(70) Koc, H.; Ozisik, H.; Deligöz, E.; Mamedov, A. M.; Ozbay, E. Mechanical, Electronic, and Optical Properties of Bi2S3 and Bi2Se3 Compounds: First Principle Investigations. *J Mol Model* **2014**, *20* (4), 2180. https://doi.org/10.1007/s00894-014-2180-1.

(71) Ren, G.-K.; Lan, J.-L.; Ventura, K. J.; Tan, X.; Lin, Y.-H.; Nan, C.-W. Contribution of Point Defects and Nano-Grains to Thermal Transport Behaviours of Oxide-Based Thermoelectrics. *npj Comput Mater* **2016**, *2* (1), 1–9. https://doi.org/10.1038/npjcompumats.2016.23.

(72) Kittel, C. *Introduction to Solid State Physics*, 8th ed.; John Wiley & Sons: New York, NY, 2004.